EarthArXiv cover page for: Direct quantification of solar-induced chlorophyll fluorescence using compact solar-blind optical radiometers

Jonas Kuhn[1,⋆] and Jochen Stutz

Department of Atmospheric and Oceanic Sciences, University of California, Math Sciences Building 7127, Los Angeles, CA 90095, USA
[1]now at: Institute of Environmental Physics, Heidelberg University, Im Neuenheimer Feld 229, 69120 Heidelberg, Germany
⋆Corresponding author: jonaskuhn-sci@posteo.de

This is a non-peer-reviewed preprint submitted to EarthArXiv.

This manuscript has been submitted for publication in Remote Sensing of Environment. Please note the manuscript has yet to be formally accepted for publication. Subsequent versions of this manuscript may have slightly different content. If accepted, the final version of this manuscript will be available via the 'Peer-reviewed Publication DOI' link on the right-hand side of this webpage. Please feel free to contact any of the authors; we welcome feedback.

Direct quantification of solar-induced chlorophyll fluorescence using compact solar-blind optical radiometers

Jonas Kuhn[1,⋆] and Jochen Stutz

Department of Atmospheric and Oceanic Sciences, University of California, Math Sciences Building 7127, Los Angeles, CA 90095, USA
[1]now at: Institute of Environmental Physics, Heidelberg University, Im Neuenheimer Feld 229, 69120 Heidelberg, Germany
⋆Corresponding author: jonaskuhn-sci@posteo.de

Abstract. Remote sensing of solar-induced chlorophyll fluorescence (SIF) provides a non-invasive, quantitative measure of plant photosynthetic activity, linking leaf-level physiology to canopy and ecosystem behavior and the global carbon cycle. Current SIF measurements rely on hyperspectral retrievals of the weak fluorescence signal from small changes in Fraunhofer lines or atmospheric absorption features in plant or canopy reflectance spectra. Because this approach is dependent on atmospheric and illumination conditions, it relies on bulky and costly instrumentation, while complex retrieval algorithms demand atmospheric spectroscopy expertise. These limitations restrict widespread proximal SIF remote sensing applications, and contribute to critical observational gaps, highlighting the need for a simplified measurement approach.

We introduce a fundamentally different approach to proximal SIF remote sensing: by measuring the light intensity within a saturated atmospheric O_2 line (ca. 10 pm spectral width) we implement a solar-blind radiometer (SBR) that optically isolates SIF from reflected solar radiation. Calculations show that SBR-SIF instruments can be implemented using a Fabry-Pérot interferometer in double-pass configuration. Plant measurements with our prototype confirm the theoretical calculations and provide direct SIF measurements with a precision of $0.1\,\mathrm{mW\,m^{-2}\,sr^{-1}\,nm^{-1}}$ in 3 minutes, similar or higher than conventional techniques. SBR-SIF is independent of atmospheric and illumination conditions, requires no spectral retrieval or reference measurement, and enables compact, field-deployable instrumentation. Consequently, SBR-SIF enables scalable proximal SIF measurements that can advance our understanding of physiological processes, support validation of satellite observations, and expand SIF applications in ecosystem monitoring and precision agriculture.

Keywords: solar-induced chlorophyll fluorescence, SIF, photosynthesis, proximal remote sensing, solar-blind radiometer, Fabry-Pérot interferometer, atmospheric oxygen.

Highlights

- Solar blind radiometry enables the direct measurement of SIF radiance.
- Solar blind radiometers can be implemented with Fabry-Pérot interferometers.
- Prototype measurements validate theory and outperform hyperspectral approaches.
- Simple and compact sensors enable scalable real-time measurements of SIF.

1 Introduction

Remote sensing of solar-induced chlorophyll fluorescence (SIF) provides non-invasive, in-situ insight into the physiology of plants in their natural environment (Meroni et al., 2009; Frankenberg

et al., 2012; Porcar-Castell et al., 2014; Frankenberg and Berry, 2017). Ground-based (proximal), air-, and space-borne SIF observations help scaling physiological processes from individual leaves or plants to ecosystems and the global scale. While SIF observations have made important contributions to studies of ecosystem behavior and atmosphere-biosphere interaction over the past decades (Porcar-Castell et al., 2014; Mohammed et al., 2019), the difficulties of measuring SIF have restricted observations to specific sites and/or conditions and hindered widespread application in areas such as crop and ecosystem monitoring.

The fundamental challenge in measuring SIF is that the fluorescence signal emitted at wavelengths between ca. 600 nm and 800 nm is masked by the much brighter sunlight reflected from vegetation. The reflected intensity exceeds that of SIF by approximately two orders of magnitude in the far-red (∼700 - 800nm) and by one order of magnitude in the red (∼600 - 700nm) wavelength range (Fig. 1A). Moreover, the absolute intensity and the spectrum of reflected light are highly variable and controlled by many different and independent environmental and observational parameters, such as cloudiness, solar geometry, and viewing geometry.
The current approach to SIF measurements, i.e. the separation of SIF from the reflected light, relies on a hyperspectral analysis that compares reflectance spectra of the plant or canopy with a plant-free reference spectrum, i.e. a direct sky or solar spectrum. The SIF signal is quantified by determining the change of optical depths of either solar Fraunhofer lines or bands of telluric oxygen absorption lines between a leaf/canopy spectrum and a skylight spectrum (Plascyk, 1975; Meroni et al., 2009; Frankenberg and Berry, 2017; Grossmann et al., 2018; Du et al., 2019). However, this approach faces a number of challenges. Both oxygen and Fraunhofer lines, which have spectral widths of only a few picometers, remain highly under-sampled by the currently used grating spectrographs. In the case of Fraunhofer line-based retrievals the insufficient spectral resolution reduces the absolute optical depth of the lines by approximately one order of magnitude. To accurately detect a SIF signal, which changes the Fraunhofer line depths by less than 1-3% in the far-red, very high signal to noise ratio (SNR) and excellent spectral stability of the instrument are needed (Grossmann et al., 2018; Chang et al., 2020; Trim and Hueni, 2025). While the optical depth of telluric oxygen bands is much larger, easing the SNR requirements, the effective optical depth of these bands exhibits a highly non-linear dependence on atmospheric radiative transfer effects, i.e., on solar position change, surface albedo, the presence of aerosol and clouds, etc. (Chang et al., 2020; Liu and Liu, 2018). In both oxygen band and Fraunhofer line based SIF observation techniques, leaf/canopy spectra and skylight spectra need to be measured in sequence with the same instrument. Atmospheric state or instrumental changes within the time gap between the two spectra can cause substantial systematic errors (Chang et al., 2020; Marrs et al., 2021; Trim and Hueni, 2025).

Highly specialized and costly satellite instruments can provide sufficient SNR and spectral stability to allow for Fraunhofer-line based global SIF retrievals. However, for proximal, i.e., ground-based SIF remote sensing, the challenges associated with the current hyperspectral approach have led to cumbersome instruments that are difficult to operate in the field (Grossmann et al., 2018), onerous calibration procedures (Trim and Hueni, 2025), and highly complex signal processing (Marrs et al., 2021). The cost and effort required and the level of expertise needed to conduct state-of-the-art hyperspectral SIF measurements limit the widespread application of proximal SIF observations in research, agriculture, and ecosystem management. As a consequence, long-term, high-temporal-resolution, and location and ecosystem specific proximal SIF data remain scarce. This scarcity of proximal SIF data contributes to persistent knowledge gaps in the relationship between SIF measurements, plant physiology, and the global carbon cycle (Porcar-Castell et al., 2014; Mohammed et al., 2019; Pierrat et al., 2025; Qin et al., 2026). These knowledge gaps, the required validation of the growing body of satellite-based SIF datasets (Drusch et al., 2017; Doughty et al., 2022), and the high potential of SIF observations to support ecosystem monitoring and agriculture, highlight the urgent need for improved and scalable prox-

imal SIF measurement techniques.

The objective of this study is to introduce a fundamentally different approach to proximal SIF remote sensing that overcomes many of the challenges of the current hyperspectral SIF measurements. The approach is based on the development of a compact solar-blind radiometer (SBR) that optically isolates the SIF signal from the light reflected by a plant or canopy. The SBR quantifies the SIF radiance directly, without relying on hyperspectral retrievals or cumbersome instrumentation. We explain the principle of SBR-based SIF measurements (SBR-SIF) and quantitatively assess the requirements for its implementation (Sect. 2). We show that these requirements can be met by recent developments in the application of Fabry-Pérot interferometers (FPIs), and demonstrate that the SBR-SIF can be implemented in a compact, robust, and low-maintenance instrument (Sect. 3). Our prototype confirms the theoretical considerations and validates the substantial advantages of SBR-SIF over current hyperspectral methods in real-world measurements (Sect. 4). In contrast to current techniques, SBR-SIF will facilitate the scalable and widespread application of accurate proximal SIF remote sensing measurements to support studies of physiological processes on leaf, plant, canopy, and ecosystem scales. Through scalability, SBR-SIF will also offer new opportunities for precision agriculture and ecosystem management applications supporting mitigation of ongoing climate-related environmental change.

2 Solar-blind radiometry in the (far-)red: A novel approach to quantifying SIF

2.1 The world inside a strong saturated oxygen line

Sunlight traverses the solar atmosphere and Earth's atmosphere before it reaches the surface. Along the way, molecules and atoms absorb a fraction of this light causing structured and species-specific imprints (absorption lines) in the solar spectrum. Aside from Fraunhofer lines, which originate from absorption in the sun's photosphere, atmospheric oxygen absorption in the O_2A ($\sim$ 762nm) and O_2B ($\sim$ 690nm) bands is among the most prominent features in sunlight spectra at the Earth's surface. Many of the individual absorption lines forming the O_2A and O_2B bands are saturated, which means that, in their center, they absorb all sunlight before it can reach the surface. This includes the strong O_2 lines of the O_2A band that overlap with the chlorophyll emission spectrum (Fig. 1A), which are the focus of our study.
Sunlight reaching a plant canopy is either reflected or absorbed. The reflectivity of plants/canopies is smooth on the spectral scale of individual O_2 absorption lines and conserves the incoming light energy, i.e., its wavelength remains unchanged during reflection. Consequently, the narrow-band spectral features, such as O_2 absorption lines, are conserved in the spectrum of sunlight reflected by vegetation (Fig. 1A). Light absorbed by chlorophyll in leaves leads to photosynthesis and the emission of SIF. Because the energy between absorbed and emitted radiation in a fluorescence process changes and energy dissipation follows a statistical process, the emitted SIF spectrum is smooth (Fig. 1A,B). Consequently, the outgoing radiance from a plant I_{plant} is the sum of the reflected radiance $I_{\text{refl.}}$, conserving the narrow-band spectral features in the incoming solar radiation, and the smooth SIF radiance I_{SIF}. In particular, SIF is emitted at wavelengths at which strong saturated atmospheric O_2 lines absorb all sunlight and, thus, no light is reflected from the plant or other nearby surfaces (Fig. 1B). In other words, narrow spectral regions $\Delta\lambda_{\text{sb}}$ around saturated O_2 line centers are "solar-blind".

To build intuition for this concept, it is instructive to imagine the solar-blind world inside a strong saturated atmospheric O_2 line of the O_2A-band at Earth's surface, which differs substantially from our everyday experience (Fig. 1C): Even during daytime hours it would be dark,

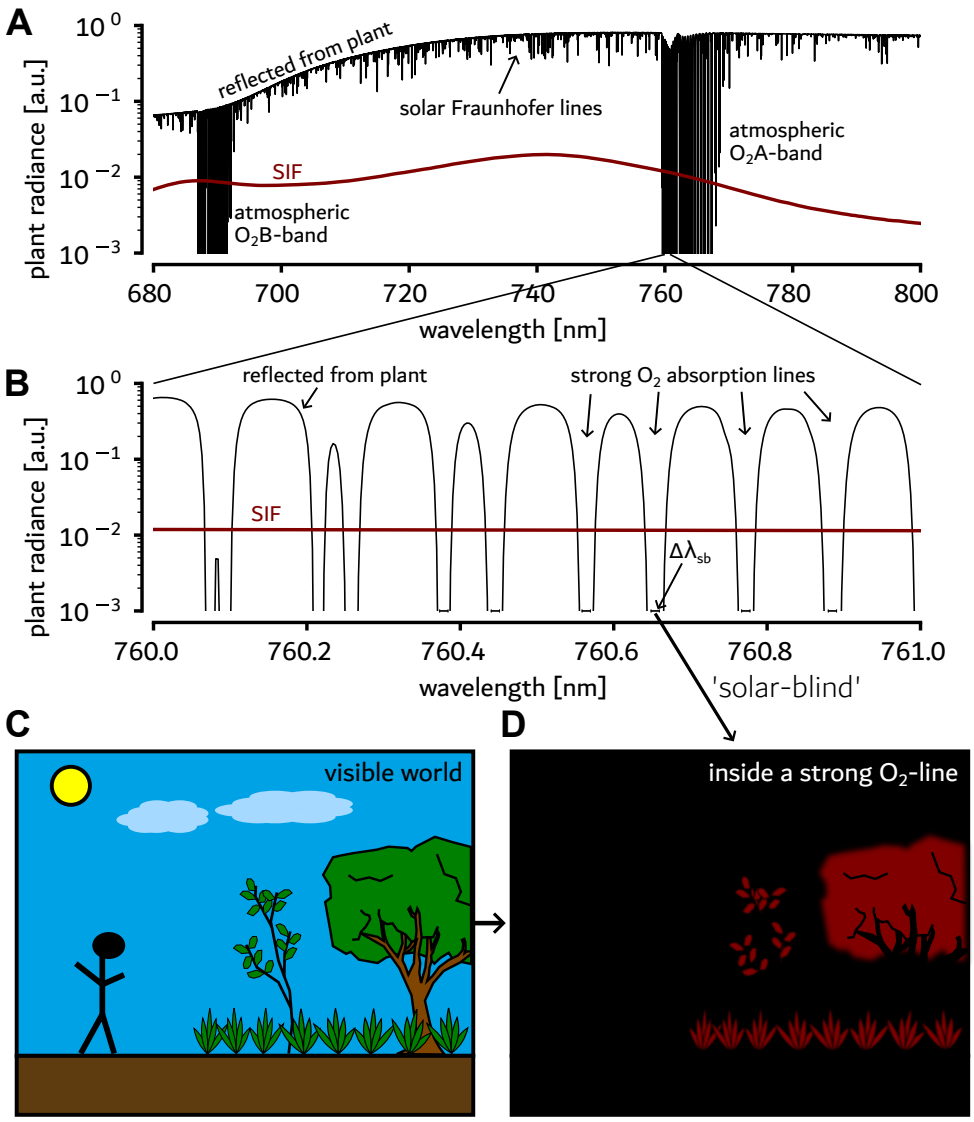

Figure 1: The radiance of reflected sunlight (black) are considerably larger than SIF (red) above a leaf or canopy in most of the (far-)red spectral range (A). Individual strong O_2 lines (B) within the atmospheric O_2A-band reduce the reflected radiance far below the SIF radiance. Consequently, under most conditions, SIF is the only light source within the solar-blind narrow wavelength ranges $\delta\lambda_{sb}$ covered by saturated O_2 lines. The 'world' (panel C) inside a strong O_2 line is visualized conceptually in panel D.

because all sunlight, moonlight, and starlight is fully absorbed by the atmosphere. The only sources of light are (1) artificial light sources, which are often turned off during the day, (2) natural thermal sources, such as fires, and (3) fluorescence, which at these wavelengths is dominated by chlorophyll. Consequently, the world inside a saturated atmospheric O_2 line would be dark with shimmering plants as the main source of light. The strong O_2 absorption furthermore limits the visibility to about 50 - 100m, thus only nearby vegetation can be seen. These considerations demonstrate the feasibility of directly quantifying SIF from nearby plants with a simple intensity measurement inside a saturated O_2 absorption line.

In the following, we further assess the underlying principles of an instrument designed to measure the light intensity within an individual saturated atmospheric O_2, i.e. implementing SBR-SIF. First, we will characterize the properties of saturated atmospheric O_2 lines in more detail.

2.2 Width of a saturated atmospheric oxygen line

In order to measure the light intensity within the narrow spectral interval $\Delta\lambda_{\mathrm{sb}}$ inside an individual strong O_2 absorption line, we first need a quantitative understanding of the spectral width of these lines. The spectral width of an O_2 line in the absorption cross section $\sigma(\lambda)$ is controlled by pressure and Doppler broadening. For oxygen at standard temperature and pressure this width is ca. 6-7 pm (Rothman et al., 2013). Atmospheric temperature and pressure variations impact this width by at most a few percent.
However, if the optical depth of the O_2 line is large and the intensity around the line center is essentially zero, i.e. the line is saturated, the effective spectral width of the line in the intensity spectrum becomes dependent on the optical depth. To determine the width of saturated atmospheric O_2 lines in solar spectra at the ground, we therefore need to calculate how the O_2 absorption changes the intensity spectrum of direct sunlight from the top of the atmosphere, I_{TOA}, to the intensity at the ground, I_{G}. We are interested in a lower estimate of the O_2 line width, and will therefore focus on direct sunlight, which follows the shortest path through the atmosphere. Scattering by aerosol and clouds makes the light path longer, further broadening the line width. Consequently, we calculate the surface solar spectrum using Beer's law for direct sunlight using the following equation:

$$I_{\mathrm{G}}(\lambda) = I_{\mathrm{TOA}}(\lambda)\, \exp\left[- \int_{\mathrm{TOA}}^{G} \mathrm{dh}\, \frac{\sigma_{\mathrm{O2}}(\lambda, \mathrm{h})\, \mathrm{c_{O2}(h)}}{\cos\phi_{\mathrm{S}}} \right] \tag{1}$$

We approximate I_{TOA} using a black body spectrum at 5800 K and Fraunhofer line data (Toon, 2015). The absorption cross section, $\sigma_{\mathrm{O2}}(\lambda, h)$, is sourced from the HITRAN database (Rothman et al., 2013) using pressure and temperature from the International Standard Atmosphere (International Organization for Standardization, 1975). The oxygen concentration profile c_{O2} is calculated from the International Standard Atmosphere density profile and the atmospheric oxygen mixing ratio. Our calculation is performed on a 1 km grid for altitudes h from the ground to 20 km, and is only accurate for solar zenith angles ϕ_{S}, of less than 75°, for which this simplified geometric approach is valid. Larger solar zenith angles will, however, always enhance the O_2 optical depth.

The results of this calculation, after multiplication with a typical plant reflectivity spectrum (Wu et al.), are shown in Fig. 1A and S2A, for the conservative case of a solar zenith angle of 0° at an altitude of 2000 m above sea level (a.s.l.). Further scenarios are shown in Fig. S1A. Our calculations show that the width of the solar-blind region within a strong saturated O_2 line is around 10 pm. This width increases by a factor of ca. 2-3, depending on the geographical location, season, time of day, or meteorological conditions. We conclude that the width $\Delta\lambda_{\mathrm{sb}}$

of the passband, i.e. the width of the transmitted wavelength interval, of an SBR capable of measuring SIF within a strong saturated oxygen line anywhere on the Earth's surface must be limited to 10 pm.

2.3 Visibility in the solar-blind regime

The visibility within a strong saturated atmospheric O_2 line, and thus the range of SBR-SIF measurements, is naturally limited by the O_2 absorption along the path from the fluorescing plant to the SIF instrument. We define the viewing range L_{sb} of the SBR as the length L at which the SIF intensity is reduced by a factor of $e^{-1} \approx 0.37$ by the O_2 absorption, i.e., the length L at which the absorption optical thickness according to Beer-Lambert's law $\tau_{\mathrm{O2}} = \log \frac{I_{\mathrm{SIF}}}{I_{\mathrm{meas.}}} = \sigma_{\mathrm{O2}} \cdot c_{\mathrm{O2}} \cdot L$ equals unity:

$$L_{\mathrm{sb}} = [\sigma_{\mathrm{O2}}\, c_{\mathrm{O2}}]^{-1} \tag{2}$$

with the emitted SIF radiance at the plant I_{SIF}, the measured radiance at distance L, I_{meas}, the O_2 concentration c_{O2}, and the O_2 absorption cross section σ_{O2} at surface conditions. L_{sb} is smallest in the O_2 line center and increases rapidly with spectral distance from center, which means that the overall influence of SIF re-absorption decreases for increasing $\Delta\lambda_{\mathrm{sb}}$. According to Eq. 2 the range L_{sb} of SBR-SIF measurements at ground level is between 30 to 50 m in the line center (Fig. S1 B). Effective values of L_{sb} can be determined for specific SBR passbands and used for the correction of longer range SIF measurements. The lower limit given by the line center values demonstrates that most proximal SBR-SIF observations are not significantly affected by SIF re-absorption through O_2.

In summary, the proposed SBR technology can provide direct SIF measurements from within a few dozens of meters by exclusively measuring the light intensity within a narrow wavelength window $\Delta\lambda_{\mathrm{sb}}$ of ca. 10 pm centered around a strong saturated O_2 line of the O_2A band. In the following section, we demonstrate that these SBR-SIF measurements can be realized using readily available optical components.

3 Implementation of solar-blind radiometry: Fabry-Pérot interferometers

3.1 Spectroscopic requirements for the implementation of an SBR

An SBR must isolate a very narrow wavelength window within a strong O_2 line while effectively suppressing all light from other wavelengths in the solar spectrum reaching Earth's surface. This solar-blind spectral window $\Delta\lambda_{\mathrm{sb}}$ corresponds to a fraction of only ca. $2{\cdot}10^{-5}$ of the entire solar spectrum. Therefore, the SBR must be capable of measuring small light intensities. The spectral light throughput of the SBR increases with $\Delta\lambda_{\mathrm{sb}}$, which should be as large as possible, while meeting the condition:

$$\int_{\Delta\lambda_{\mathrm{sb}}} I_{\mathrm{SIF}}\, \mathrm{d}\lambda > \kappa \int_{\Delta\lambda_{\mathrm{sb}}} I_{\mathrm{refl.}}\, \mathrm{d}\lambda \tag{3}$$

with the SIF intensity I_{SIF}, the intensity of reflected light $I_{\mathrm{refl.}}$ (Fig. 1B), and the targeted suppression κ of reflected light within $\Delta\lambda_{\mathrm{sb}}$. In our assessment of the width of an atmospheric O_2 line (Sect. 2) we found that 10 pm is a conservative, but reasonable, choice for $\Delta\lambda_{\mathrm{sb}}$. For instance, according to Eq. (3), κ is on the order of 10^{-8} for the strong O_2 absorption line at 760.65 nm assuming an SZA of 0° and 4000 m a.s.l. However, when choosing the weaker O_2 line at 761.82 nm, for the same conditions, κ would be as large as 10%, preventing accurate SBR measurements. The relationship between κ and $\Delta\lambda_{\mathrm{sb}}$ is highly non-linear. For example, doubling $\Delta\lambda_{\mathrm{sb}}$ would reduce κ at 760.65 nm by 7 orders of magnitude. For most SBR-SIF applications

κ should be at most 0.01, so that the influence of reflected light from within $\Delta\lambda_{sb}$ on the SIF signal is reduced to 1%.

This study focuses on the implementation of a universal SBR at 760.65 nm therefore using the rather conservative value of $\Delta\lambda_{sb} = 10\,\text{pm}$.

Because at 760 nm the SIF signal is only ca. 1% of the reflected radiance and $\Delta\lambda_{sb}$ covers only a fraction of ca. $2{\cdot}10^{-5}$ of the spectrum of reflected solar light, the SBR requires exceptional spectroscopic performance:

- The SBR has to suppress all light from outside $\Delta\lambda_{sb}$.
- The spectral light-throughput of the SBR has to be high enough to enable measurements on the same time scale as the observed process.
- The spectroscopic setup must be suitable for long-term, low-maintenance operation under versatile and harsh field conditions.

The passband, or resolved spectral interval $\delta\lambda$, of a spectral filter or monochromator is typically defined as the full spectral width at half maximum transmittance (FWHM). However, for the implementation of an SBR the transmittance in the wings of the passband is crucial because the contribution of reflected light rapidly increases with the distance from the absorption line center (Fig. S2A). In order to fulfill the condition in Eq. (3), $\delta\lambda_{SBR}$ needs to be smaller than $\Delta\lambda_{sb}$ and the contrast of the passband needs to be high, i.e. very small transmittance in the wings (see Fig. 1B).

The spectral light-throughput, k (in units of $\text{sr}\,\text{mm}^2\,\text{nm}$), is defined as the instrument characteristic that relates the radiance I, e.g. that emanates from a canopy, (in units of photons $\text{s}^{-1}\,\text{sr}^{-1}\,\text{mm}^{-2}\,\text{nm}^{-1}$) to the rate J of photons detected by the instrument within the spectral interval $\delta\lambda$ (in units of photons s^{-1}, see Kuhn et al., 2021, 2023):

$$J = k(\delta\lambda) I_{\text{plant}} = E(\delta\lambda)\,\delta\lambda\,\gamma\,I_{\text{plant}} \tag{4}$$

The instrument geometrical beam acceptance or etendue, E, is given by the product of the surface area of the accepted beam cross section A (in mm^2) and its solid angle Ω (in sr). The factor γ accounts for loss at optical components.

Accordingly, the number of SIF photons N_{SIF} detected by an SBR within an exposure time of δt is given by:

$$N_{SIF} = J\,\delta t = E(\delta\lambda_{SBR})\,\delta\lambda_{SBR}\,\gamma\,I_{SIF}\,\delta t \tag{5}$$

Using Eq. 5, we can derive the etendue requirements of an SBR for SIF measurements. For example, we can assume an exposure time of $\delta t = 10\,\text{s}$, optical loss $\gamma = 0.1$, $\delta\lambda_{SBR} = 0.3{\cdot}\Delta\lambda_{sb} = 0.0033\,\text{nm}$, $I_{SIF} = 3 \cdot 10^9$ photons $\text{s}^{-1}\,\text{sr}^{-1}\,\text{mm}^{-2}\,\text{nm}^{-1}$, corresponding to a typical SIF radiance of slightly less than $1\,\text{mW}\,\text{sr}^{-1}\,\text{m}^{-2}\,\text{nm}^{-1}$ (Grossmann et al., 2018), and $N_{SIF} = 1000$ detected photons to dominate typical photo-detector noise levels and achieve a signal to noise ratio (SNR) on the order of 30. For this case the SBR requires an etendue of $E = 10^{-4}\,\text{mm}^2\,\text{sr}$.

Many classic monochromator setups, such as those based on gratings, cannot meet these requirements in field-deployable instruments, because their etendue, and hence their light throughput, decreases rapidly for higher spectral resolution (see Supplement S2). Fabry-Pérot interferometers, on the other hand, are known to provide high light throughput at high spectral resolution and contrast in compact and robust optical setups (Jacquinot, 1954; Vaughan, 1989; Kuhn et al., 2021, 2023).

3.2 SBR-SIF implementation with Fabry-Pérot interferometers

3.2.1 Spectral resolution and light throughput of FPIs

Fabry-Pérot interferometers (FPIs) have been used in optical spectroscopy since the late 19th century (Perot and Fabry, 1899; Vaughan, 1989). They represent a fundamentally simple optical

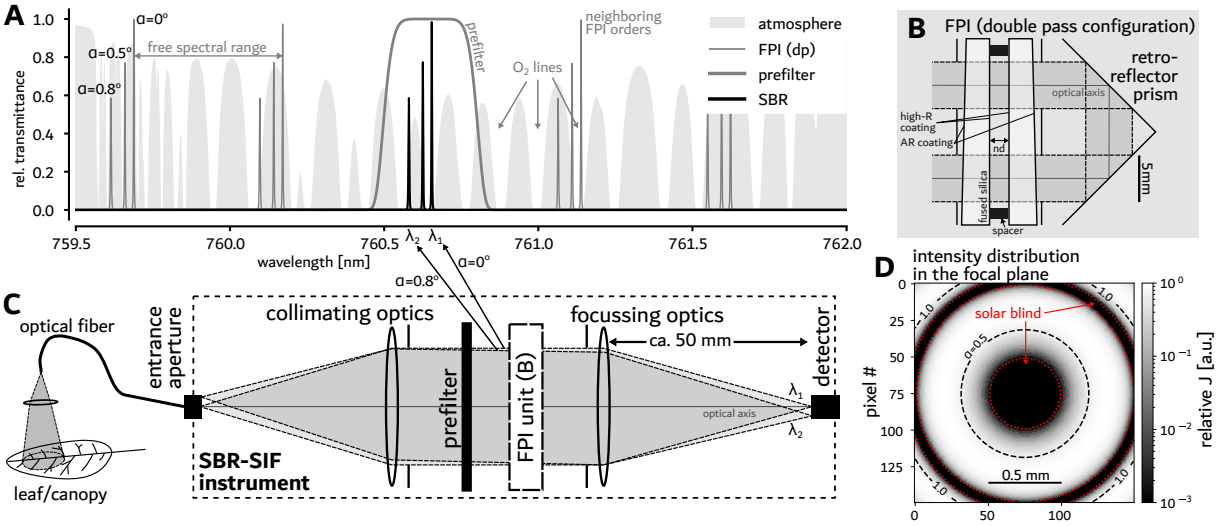

Figure 2: A: The transmittance spectrum of an FPI in double pass configuration (B) with constant optical separation of the mirrors is shifted towards lower wavelength with increasing incidence angle α of the light onto the FPI (thin gray line for 3 values of α). For a constant beam divergence, the peak transmission decreases, while $\delta\lambda_{\mathrm{FPI}}$ slightly increases (Kuhn, 2015; Kuhn et al., 2023). In the proposed SBR-SIF instrument (C) an entrance optic directs light from a leaf or canopy to the entrance aperture, which is imaged by a collimating and a focusing optics to the instruments focal plane. The prefilter and the FPI are placed within the collimated part of the beam, so that different incidence angles α, i.e., different transmitted wavelength, are mapped onto different locations in the focal plane. The solar-blind regions in the focal plane (D), in which the FPI transmittance overlaps strong O_2 lines can be isolated with apertures or resolved with a camera detector.

device, only consisting of two plane-parallel surfaces (mirrors) of reflectivity R, separated by an optical distance $n\,d$, with physical separation d and refractive index n (Fig. 2B). Light with incidence angle α towards the optical axis, is reflected back and forth between the two mirrors, transmitting a fraction (of roughly 1-R) of the beam after each cycle. Superposition of these transmitted partial beams determines the effective transmittance spectrum of the FPI, which consists of periodic peaks of maximum transmittance caused by constructive interference (Fig. 2A). The reflectivity, quality, and alignment of the mirrors determine the FPI's finesse F, which describes the ratio of the width of a transmittance peak to its free spectral range. The free spectral range describes the spectral separation of two transmittance maxima and depends on the phase difference between two consecutively transmitted partial beams and thus on their optical path difference $\Gamma = 2nd\cos\alpha$. The transmittance spectrum $T_{\mathrm{FPI,s}}$ of an ideal, parallel light beam is described by the Airy function (for $F > 1$, e.g., Vaughan, 1989):

$$T_{\mathrm{FPI,s}}(\lambda, \alpha, n, d) = \left(1 + \frac{4\,F^2}{\pi^2}\,\sin^2\left(\pi\frac{\Gamma(n,d,\alpha)}{\lambda}\right)\right)^{-1} \tag{6}$$

For higher orders $m = \frac{\Gamma}{\lambda}$, small variations in n, d, or α cause a shift of the spectral transmission (Fig. 2A). Hence, the effective transmittance spectrum of a realistic, not ideally parallel, light beam covering a solid angle Ω is given by the integral (e.g. Kuhn, 2015; Lv et al., 2024):

$$T_{\mathrm{FPI}}(\lambda, \alpha, n, d) = \int_{\Omega} T_{\mathrm{FPI,s}}(\lambda, \omega, n, d)\,\mathrm{d}\omega \tag{7}$$

Consequently, the incidence angle dependence of $T_{\mathrm{FPI,s}}$ determines the maximum beam solid angle for a given spectral resolution $\delta\lambda_{\mathrm{FPI}}$ of the FPI, i.e., the FWHM of an individual FPI transmission peak. If this beam solid angle Ω_{FPI} is exceeded, the effective FPI peaks will smear out and $\delta\lambda_{\mathrm{FPI}}$ will increase. The relation between Ω_{FPI} and $\delta\lambda_{\mathrm{FPI}}$ is given by (see, e.g.,

Jacquinot, 1954; Vaughan, 1989; Kuhn et al., 2021):

$$\Omega_{\mathrm{FPI}} = 2\pi \frac{\delta\lambda_{\mathrm{FPI}}}{\lambda} \tag{8}$$

The etendue of an FPI able to resolve $\delta\lambda_{\mathrm{FPI}}$ is thus given by:

$$E_{\mathrm{FPI}} = \Omega_{\mathrm{FPI}}(\delta\lambda_{\mathrm{FPI}}) \cdot A_{\mathrm{FPI}} \tag{9}$$

with the FPI clear aperture surface area A_{FPI}. From Eq. 8 and 9 we can derive that, for a resolution of $\delta\lambda = 0.0033\,\mathrm{nm}$ at 760 nm, the FPI clear aperture surface area $\mathrm{A_{FPI}}$ required to achieve an etendue of $E_{\mathrm{FPI}} = 10^{-4}\,\mathrm{mm^2\,sr}$ (Sect. 3.1 and Eq. (9)) is ca. $4\,\mathrm{mm^2}$. Whether an FPI with this, or a larger, clear aperture can be manufactured depends on the required finesse, which we will assess next.

3.2.2 Finesse requirements for SBR

In order to exploit the FPI's spectroscopic advantages in a monochromator-type setup, an individual FPI transmission order must be isolated with a prefilter. The passband width, or spectral resolution, $\delta\lambda_{\mathrm{PF}}$ of the prefilter needs to be smaller than the free spectral range of the FPI (Fig. 2A), so it sufficiently suppresses the radiance transmitted by neighboring FPI orders. The availability of narrow-band prefilters thus determines the minimum free spectral range $\Delta\lambda_{\mathrm{FPI}}$ of the FPI, which, through the FPI's finesse, determines the spectral width $\delta\lambda_{\mathrm{FPI}}$ of an FPI transmission peak (see Kuhn et al., 2021, for details):

$$\delta\lambda_{\mathrm{PF}} \approx \Delta\lambda_{\mathrm{FPI}} = F\,\delta\lambda_{\mathrm{FPI}} \approx \frac{\lambda^2}{\Gamma} \tag{10}$$

Different optical components, such as additional lower resolution FPIs, interference band-pass filters, or grating monochromators, can be used as prefilters (Vaughan, 1989; Kuhn et al., 2021). For example, state-of-the-art compact grating monochromators or interference filters provide a passband of $\delta\lambda_{\mathrm{PF}} = 0.3\,\mathrm{nm}$. For our conservative SBR implementation ($\delta\lambda_{\mathrm{FPI}} = 0.0033\,\mathrm{nm}$), we could choose an FPI with a free spectral range of 0.5 nm (d = 0.5 mm). Then, according to Eq. 10, a finesse of $F \approx 150$ is required. For wavelength around 760 nm, FPIs with a finesse of 150 are readily available with a clear aperture surface area of ca. $20\,\mathrm{mm^2}$, exceeding the requirement of $\mathrm{A_{FPI}} \approx 4\,\mathrm{mm^2}$ (Sect. 3.2.1).

3.2.3 FPI contrast enhancement

The spectral shape of an individual FPI transmittance peak is described by a Lorentzian function (Vaughan, 1989), and therefore its wings fall off relatively slowly with wavelength. Consequently, an FPI with $\delta\lambda_{\mathrm{FPI}} = 0.0033\,\mathrm{nm}$ still transmits too much light in the wings, where the reflected light from plants drastically increases (see Fig. S2). Because further reducing $\delta\lambda_{\mathrm{FPI}}$ would critically reduce the light throughput, this problem is best solved by using the FPI in a multi-pass configuration (Vaughan, 1989). In this configuration the light beam traverses the same FPI multiple times. For p traverses the effective FPI transmittance spectrum is then $(T_{\mathrm{FPI}})^p$, which leads to a strong suppression of the transmittance in the wings, thus enhancing the contrast of the individual FPI transmittance peaks. Our calculations show that a double-pass configuration ($p = 2$), implemented with a corner cube retro-reflector (Fig. 2B), is sufficient to fulfill the SBR requirements (Sect. 3.1) using an FPI with the dimensions and characteristics determined in the previous sections (see also Supplement S3).

3.3 The use of FPIs in compact and robust SBR setups

Recent advances in FPI manufacturing and photo-detector technology led to significant improvements of the optical performance and instrument design capabilities compared to the use of FPIs some decades ago (e.g. Plascyk, 1975). Currently, the most robust and thermally stable implementation of an FPI is an air-spaced etalon (ASE) with low thermal expansion glass spacers separating two glass plates. The inner surfaces of these plates have a reflective coating, while the outer surfaces are slightly wedged and have an anti-reflective coating. Such ASEs show excellent thermal and mechanical stability and have been used before in field measurements under harsh environmental conditions, without the need for thermal stabilization (Fuchs et al., 2021; Kuhn et al., 2023). Today, ASEs with the properties required for the implementation of SBR-SIF, i.e. $F \approx 150$ over a clear aperture of up to 5 mm diameter and 0.5 mm mirror separation (Eq. 10) are straightforward to manufacture.

The spectral properties of these stable FPIs can be exploited in various ways, depending on the arrangement of the optical system (Vaughan, 1989). One configuration that enables particularly compact and robust setups relies on mapping light of different FPI incidence angle α onto different locations in the focal plane. Traditionally, this configuration was called the 'photographic' use of FPIs (Jacquinot, 1960; Fabry and Buisson, 1908) and uses no moving parts. Today, the implementation of this configuration has become much easier with the availability of current camera detector technology, highly stable ASEs, and compact grating spectrometers and sub-nm interference filters serving as prefilters.

This static and compact setup, as described in detail by Kuhn et al. (2021), is the foundation of our SBR-SIF implementation. A sketch of this setup is shown in Figure 2C. An entrance optics directs light from the canopy to the entrance aperture of the SBR. The cross section of the entrance aperture is then imaged by collimating and focusing optics onto the focal plane of the SBR. The FPI is placed within the collimated beam, i.e., after the collimating optics, so that different light incidence angles α are mapped on different locations (concentric rings) in the focal plane. The prefilter (e.g. a grating or a band-pass filter) can be placed at various locations within the setup, for instance in the collimated beam next to the FPI (Fig. 2C) or at the entrance or exit optics. Different regions in the focal plane then correspond to different wavelengths according to the α-dependence of the prefiltered FPI transmittance peaks (Fig. 2A). Regions where an FPI transmittance peak overlaps saturated O_2 lines are solar-blind (Fig. 2D). Based on this principle, the SBR instrument can be implemented in different ways:

1. *Monochromator SBR*: An exit aperture isolates the solar-blind area in the focal plane, resulting in a monochromator-type SBR with a single-element detector, such as a silicon avalanche photodiode, measuring the SIF intensity after the exit aperture. This implementation is desirable, as it produces an electrical signal directly proportional to the SIF intensity. However, this setup may require accurate fine-tuning of the FPI, so that FPI transmittance and O_2 line overlap at $\alpha \approx 0°$, or the use of ring-shaped apertures. Moreover, high stability of the FPI and the other optical components is needed, which may require the stabilization of the gas density inside the ASE, for example by hermetic sealing (see Supplement S4).

2. *Single-order spectrographic SBR*: A two-dimensional detector array, such as those in CCD or CMOS cameras, placed in the focal plane allows the recording of images of the intensity distribution, such as the one shown in Fig. 2D. In this implementation, solar-blind pixels can be easily identified and their signal can be averaged. Slight changes in the FPI, for example introduced by pressure or temperature changes, can be traced and corrected in real-time by simple image processing techniques. While the retrieval of the SBR-SIF signal from a camera detector introduces an additional, albeit trivial, processing step, the single-order spectrographic SBR is easy to implement and allows for tracing and correcting instrumental changes.

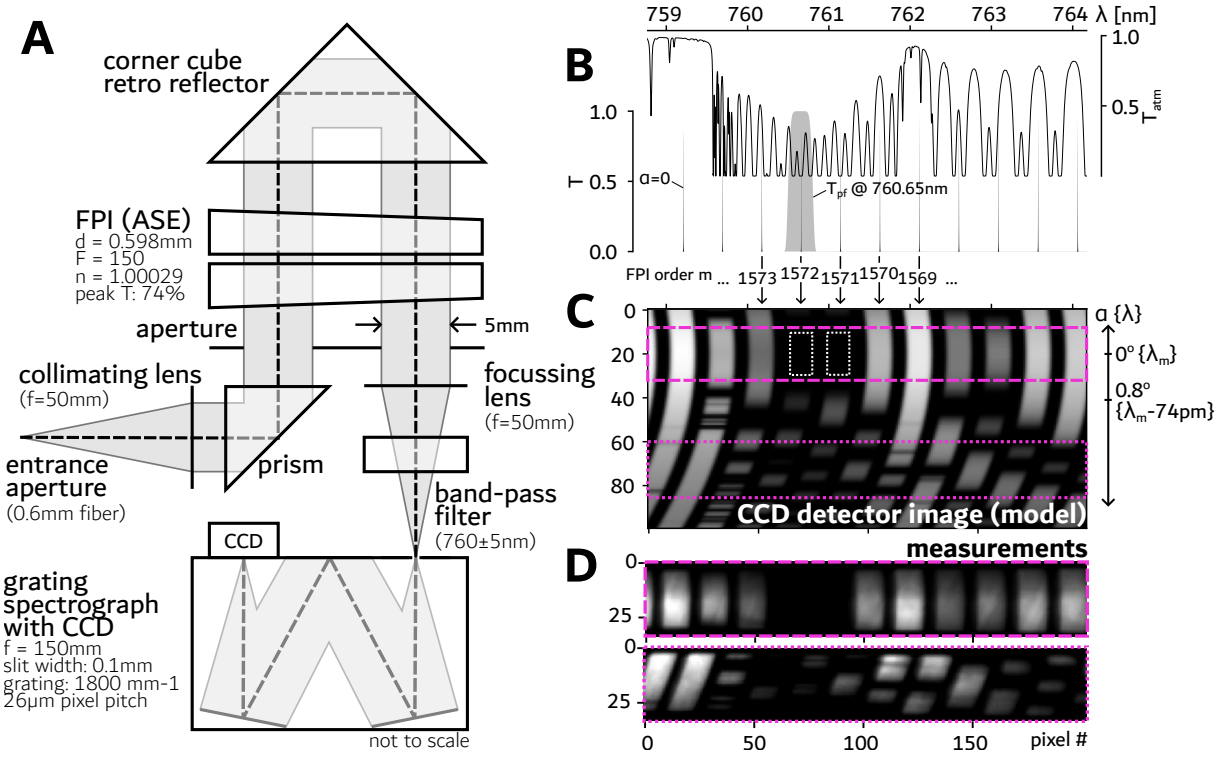

Figure 3: A: Schematic of the SBR-SIF prototype setup (not to scale) with annotated dimensions. After traversing the FPI twice, a grating spectrometer separates the individual FPI orders along the grating dispersion dimension on the CCD detector in the focal plane (B, C). In the other (here vertical) detector dimension, the FPI incidence angle α increases steadily, thereby sampling a small wavelength range. Panel C shows the simulated relative intensity distribution on the detector for direct sunlight at 0 m a.s.l. and SZA = 50°, with clearly visible O_2 absorption lines. Panel D shows two measurements with the prototype in excellent agreement with the simulation (see marked areas in C). For $\alpha = 0°$, two consecutive FPI orders coincide with strong O_2 lines causing large solar blind detector regions (enclosed by white dotted lines in C).

3. *Multi-order spectrographic SBR*: This setup is similar to the single-order spectrograph SBR-implementation, but uses a dispersive element, such as a grating spectrograph, at the exit aperture to spatially separate different FPI orders on the two-dimensional detector array in the focal plane. In this cross-dispersion configuration different FPI orders are aligned along the grating dispersion dimension on the detector. Each order represents a high resolution spectrum in cross-dispersion direction, i.e. along the dimension of the grating spectrometers entrance slit, through the α-dependence of the FPI transmittance spectrum. In other words, each FPI order represents a rectangular cut-out of the size of the grating spectrographs entrance slit of the ring-shaped intensity distribution shown in Fig. 2D (see Kuhn et al. (2021, 2023) for a detailed description).
Consequently, high resolution spectra corresponding to several FPI transmittance orders can be measured simultaneously. While this setup is optically more complex, the increased wavelength coverage of the multi-order spectrographic SBR implementation can provide important additional information, such as the light intensity outside of the O_2A-band. For this reason it was selected for the first SBR-SIF prototype.

4 Proof of concept: SBR-SIF prototype measurements

4.1 Optical setup of the SBR-SIF prototype

To demonstrate the feasibility of SBR-SIF measurements, we built a prototype instrument based on the multi-order spectrographic SBR implementation. The schematics of the prototype are shown in Fig. 3A, including relevant dimensions of the individual components.

The entrance optics of the prototype consist of a 600 μm diameter, 5m long, glass fiber that can be pointed at different targets. The exit of the fiber serves as the entrance aperture of the SBR. A lens collimates the light beam from the fiber exit. Using a prism, the collimated beam is directed through the FPI (ASE manufactured by SLS Optics Ltd.), then reversed, laterally offset, and directed through the FPI again by a corner cube retro reflector, resulting in a double pass configuration. The beam exiting the FPI is focused onto the entrance slit of a grating spectrograph (Princeton Instruments SP-2-150i) with a CCD camera (Princeton Instruments PIXIS 256B, operated at -50°) in its focal plane. A 10 nm wide band-pass filter in front of the grating spectrograph's entrance slit is used to reduce straylight.

As described above, this setup causes the orthogonal alignment of the grating dispersion and the incidence angle (α) dependence of the FPI transmittance that leads to the isolation of individual FPI orders of the detector. In order to better understand the behavior of the SBR-SIF prototype, we performed numerical simulations of the intensity distribution on the detector, based on the specifications of the optical components and the sunlight spectra calculated above (see Kuhn et al., 2021, 2023, and Supplement S5 for details). In the simulations we assumed a larger entrance aperture to better visualize the instrument behavior. Figure 3C shows the simulated relative intensity distribution on the prototype's detector for direct sunlight at sea level with a solar zenith angle of 50°, which approximates noon conditions in early February in Los Angeles, CA, USA.

The individual FPI orders are arranged in the grating dispersion direction on the CCD detector (horizontal dimension in Fig. 3C). Each FPI order (numbered in Fig. 3B) causes a vertical bright stripe with a slight curvature. The incidence angle α changes along the stripe direction (here vertical). The curvature reflects the spectral shift of the individual FPI transmittance peaks for increasing α in the grating dispersion direction, i.e. the stripe bends towards lower wavelengths when moving vertically away from perpendicular incidence ($\alpha = 0°$). The α dependence of an individual transmittance peak, or FPI order, leads to the sampling of a highly-resolved spectrum along each stripe. The effective dispersion of the FPI, i.e. the wavelength shift of a transmission maximum due to a change in α, decreases with increasing α according to the cosine dependence of the FPI optical path difference (see Eq. 6). Individual O_2 absorption lines of different strengths are clearly visible in Figure 3C. Two neighboring orders of the FPI (order 1571 and 1572) overlap with saturated O_2 lines at 760.65 nm and 761.15 nm (Fig. 2B) for $\alpha = 0°$, where the FPI's angular dispersion is highest. The saturated centers of these O_2 lines cover a larger region on the focal plane detector (marked by dotted white lines in Fig 3C). These areas are solar-blind in the manner described above and will therefore be used for SBR-SIF measurements.

4.2 Measurements

Measurements to demonstrate the SBR-SIF concept and to test the prototype were carried out at the University of California, Los Angeles during February 2026 with the prototype instrument located in the roof-top laboratory. The optical fiber entrance optics was used to directly observe reflective targets and plants placed outdoors on the roof.

4.2.1 Spectroscopic performance and high-resolution O_2 observations

Measurements pointing the optical fiber at a non-fluorescing diffuser (Spectralon) illuminated by direct sunlight during noon in Los Angeles on February 8, 2026 (Fig. 3D) were performed to

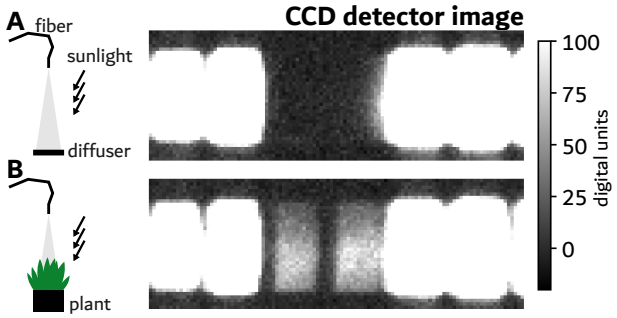

Figure 4: SBR detector images (see Fig. 3D) with the fiber pointed towards a non-fluorescing diffuser plate (A) and a small succulent plant (B), both exposed to sunlight. In the case of the diffuser plate, the light intensity in the solar-blind detector areas remain absolutely dark. With the plant, a strong light signal is visible caused exclusively by SIF photons. The images show raw data, without any digital processing apart from the subtraction of the CCD's electronic offset.

confirm the simulated intensity distribution on the detector (Fig. 3C) and therefore the prototype's spectral performance. Because the entrance aperture, i.e. the fiber cross-section, limits the vertical dimension of the detected spectral image in the prototype, two sections covering different ranges of α were measured by slightly tilting the FPI (dashed and dotted magenta boxes in Figures 3C and D). The two measured sections exactly reproduce the simulated intensity distribution in the SBR prototype's focal plane, thus confirming the theoretical framework underlying the numerical simulations. The measured sections represent O_2-A band spectra with a resolving power between more than 300.000 (at $\alpha \approx 0°$) and 150.000 (at $\alpha \approx 1.15°$), fully resolving individual O_2 lines. The prototype thus meets the spectroscopic requirements to perform SBR-SIF measurements.

4.2.2 The direct measurement of SIF in solar-blind detector regions

After establishing that the prototype functions as an SBR, we proceeded to test its capability to measure SIF. For this purpose, we compare the solar-blind region of the SBR prototype of two different measurements: (1) with the fiber pointing to a non-fluorescing diffuser and (2) with the fiber pointing to a small succulent plant (Gasteraloe beguinii). Both targets were illuminated by direct sunlight (Fig. 4). The measurements shown here were performed in direct sequence with 5 min exposure time and the fiber field of view covered entirely by the respective target. As expected from Figure 2D, when the fiber points to the diffuser, the solar-blind region on the detector remains dark, i.e. indistinguishable from non-illuminated detector regions (Fig. 4A). However, if the diffuser is replaced by the plant, we observe a clear light signal in the solar-blind regions on the SBR detector (Fig. 4B). The comparison of the two measurements in Fig. 4 provides direct evidence that the light from within the solar-blind detector regions is emitted by the plant. This light emission can only be explained by SIF and thus confirms the SBR-SIF principle and proves the feasibility of its implementation.

We can now quantify the SBR-SIF radiance solely using the plant measurement shown in Figure 4B. To improve the signal to noise ratio of the SIF measurement, we average the intensity over 10 by 20 pixel within the solar-blind detector region. To correct for the detector's dark signal, which is dominated by the electronic offset of the CCD, we subtract the average value of a nearby non-illuminated detector region. The resulting signal is directly proportional to SIF emitted by the plant and can be radiometrically calibrated, i.e., converted into a radiance. It should be emphasized that the diffuser measurement (Fig. 4A) is not needed for this analysis, because the intensity in the solar blind target area equals that of the detector's dark signal.

For the plant measurement shown in Fig. 4B, the averaged and dark-signal-corrected SIF intensity is 57.70±0.56 digital units (DU). Applying the radiometric calibration factor of 15.7 mW m^{-2}

$sr^{-1}\,nm^{-1}\,s\,DU^{-1}$ (Supplement S6) results in a radiance of $3.02\,mW\,m^{-2}\,sr^{-1}\,nm^{-1}$. This measurement and data analysis demonstrates that the SBR prototype provides SIF data with a simple, direct intensity measurement, only requiring the two basic processing steps of a dark signal correction and calibration.

4.2.3 SIF measurements during a dark-to-light transition (Kautsky effect)

To further confirm the SBR-SIF principle we measured the SBR-SIF signal during a dark-to-light transition experiment similar to the classic laboratory experiment by Kautsky and Hirsch (1931). However, instead of actively excited chlorophyll fluorescence we use SIF. The experiment has shown that the physiological processes, which effectively quench the fluorescence, require a time period of a few minutes to adapt to the sudden increase in radiation during the dark-to-light transition. Consequently, after a dark-adapted plant is suddenly exposed to light, a high fluorescence intensity is expected, which gradually decays to a steady state within minutes. This is referred to as the Kautsky effect (Kautsky and Hirsch, 1931; Lichtenthaler and Rinderle, 1988; Porcar-Castell et al., 2014). The observation of the Kautsky effect has provided evidence for the measurement of SIF by conventional methods (Grossmann et al., 2018).

We use the small succulent plant from the experiment in Section 4.2.2, which has the advantage of providing a static target not influenced by wind. The plant was covered and shielded entirely from sunlight for about 30 minutes with blackout fabric, so that it could adapt to darkness. The fiber connected to the SBR was pointed at the plant and not moved during the entire experiment, which was conducted in bright sunlight and consisted of 4 stages (Fig. 5B): In Stage I, the plant and the fiber were covered. Stage II starts after the cover of the fiber and the plant had been removed. In Stage III, a non-fluorescing diffuser was held in front of the fiber, before the fiber was covered again in Stage IV. In order to resolve the process temporally, we set the exposure time of the SBR's CCD detector to 5 s

As outlined in Section 4.2.2, we calculated the average intensity within the a solar-blind region and corrected it by the intensity of a nearby non-illuminated detector region in order to account for offset drifts (see Fig. 5A for the specific detector regions). In addition, we simultaneously trace the intensity of outgoing light from the plant, which is dominated by reflected sunlight. Here we use light close to 759.2 nm and refer to it as I_{759} (see Fig. 5A for the specific region). SBR-SIF and I_{759} were radiometrically calibrated.

The time series of SBR-SIF and I_{759} and their ratio are shown in Fig. 5B-D for exposure times of 5 s and 20 s (through co-adding of 4 detector images), respectively. At the beginning (Stage I) and the end (Stage IV) the fiber is covered so no light can enter, and SBR-SIF and I_{759} scatter around zero, showing that our dark-signal correction is accurate. Stage II marks the time period after the plant was uncovered (t=0 s) and, thus, suddenly exposed to bright sunlight. We observe a clearly visible, strong SBR-SIF intensity exceeding $6\,mW\,m^{-2}\,sr^{-1}\,nm^{-1}$, which decays on the expected time scale of a few minutes to a stable SIF radiance of ca. $3\,mW\,m^{-2}\,sr^{-1}\,nm^{-1}$. The reflected light intensity from the plant, I_{759}, on the other hand, is stable or slightly increases during the experiment. The diffuser measurement (Stage III) further confirms the fluorescence detection by increasing I_{759} while the SBR-SIF signal vanishes, reproducing the measurements shown in Fig. 4A. The measurement of the SIF Kautsky effect with our prototype further confirms the validity of the SBR-SIF approach by observing a well-known plant-physiological phenomenon.

4.2.4 Detection limit and stability of the prototype

In order to demonstrate the stability of the SBR-SIF prototype, we recorded a ca. 5 hour long SBR-SIF time series with the fiber pointed at a non-fluorescing diffuser plate that faced the sky. The measurement period encompasses broken cloud conditions with variations of the sky radiance of more than an order of magnitude, as well as clear skies (Fig. 6A). The SBR-SIF signal

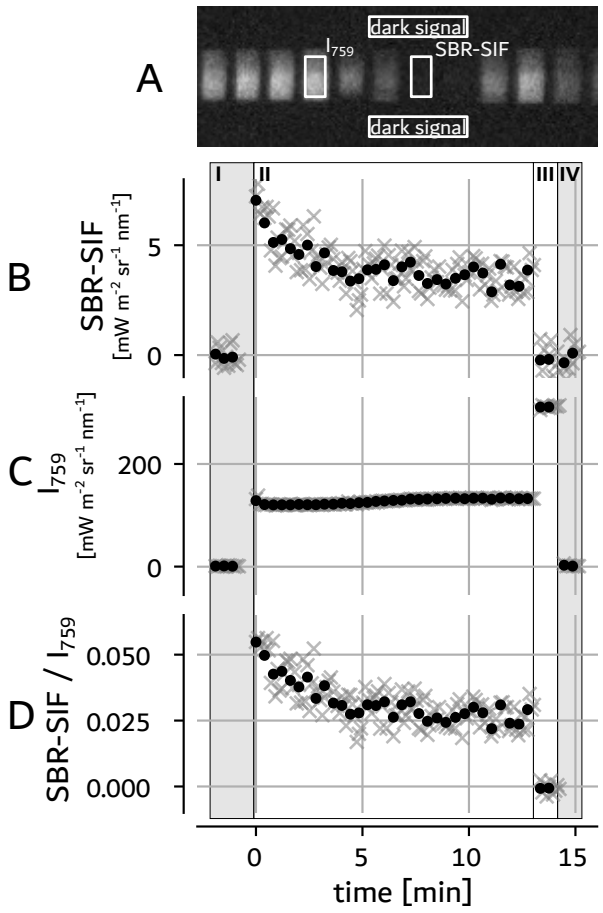

Figure 5: A: Averaging the counted photo-electrons in the solar-blind detector region and correcting for the CCD's dark signal using non-illuminated detector regions yields the SBR-SIF signal. We also trace a reference light intensity at ca. 759 nm outside the O_2A-band, which is determined by light reflection. Panels B - D show time series of the SBR-SIF intensity, the reference intensity (I_{759}) and their ratio during an experiment, in which the SBR instrument pointed at a plant that was entirely shielded from sunlight (for ca. 30 min) and then, at t=0 min (Stage II), suddenly exposed. Gray crosses correspond to measurements with an exposure time of 5 s, black dots show the mean of 4 consecutive measurements (ca. 20 s exposure). As expected from laboratory measurements (Kautsky and Hirsch, 1931), a strong SIF intensity decaying over minutes represents the accommodation of plant photosynthesis to the sudden increase light availability. During Stage I and IV the fiber was covered. During Stage III a non-fluorescent diffuser was placed in front of the fiber, which reproduces the measurement of the diffuser shown in Fig. 4A.

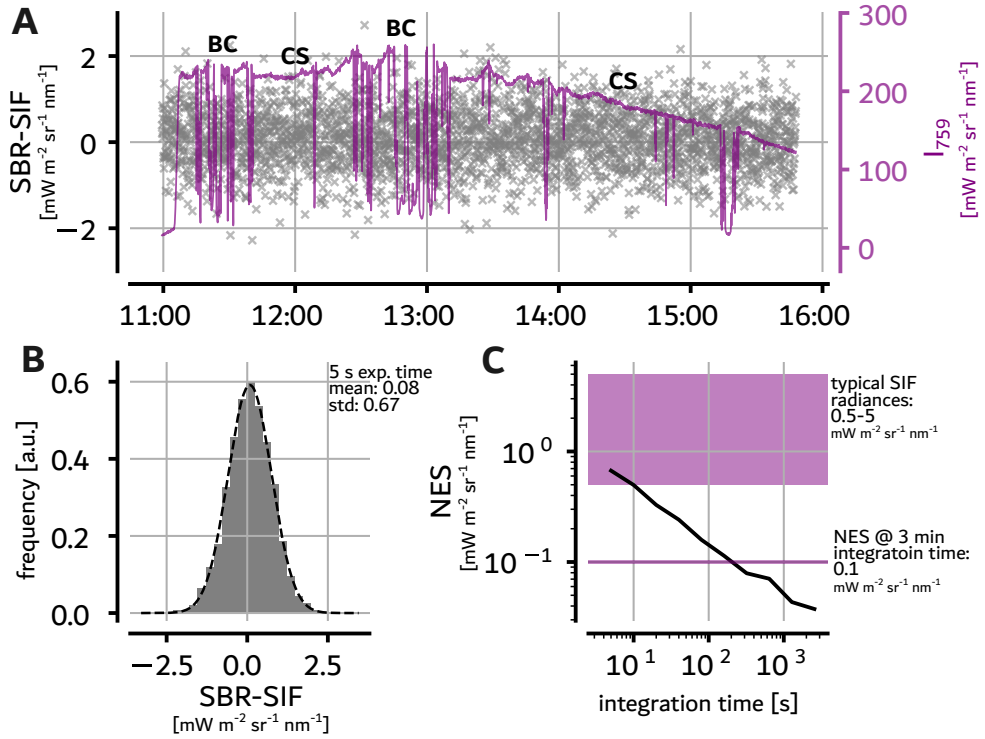

Figure 6: A: SBR-SIF measurement of a non-fluorescent diffuser plate with 5 s exposure time over ca. 5 hours during clear sky (CS) and broken cloud (BC) conditions with rapidly varying incoming sunlight, as traced by I_{759} (purple line, right ordinate axis). The corresponding histogram with the overlay of the corresponding Gaussian distribution and Allan-plot (C) demonstrate the stability of the technique and confirm that the detection limit of the SBR-SIF prototype is determined by the prototype's detector noise. The noise-equivalent signal (NES) for 3 min integration time is 0.1 mW m^{-2} sr^{-1} nm^{-1}.

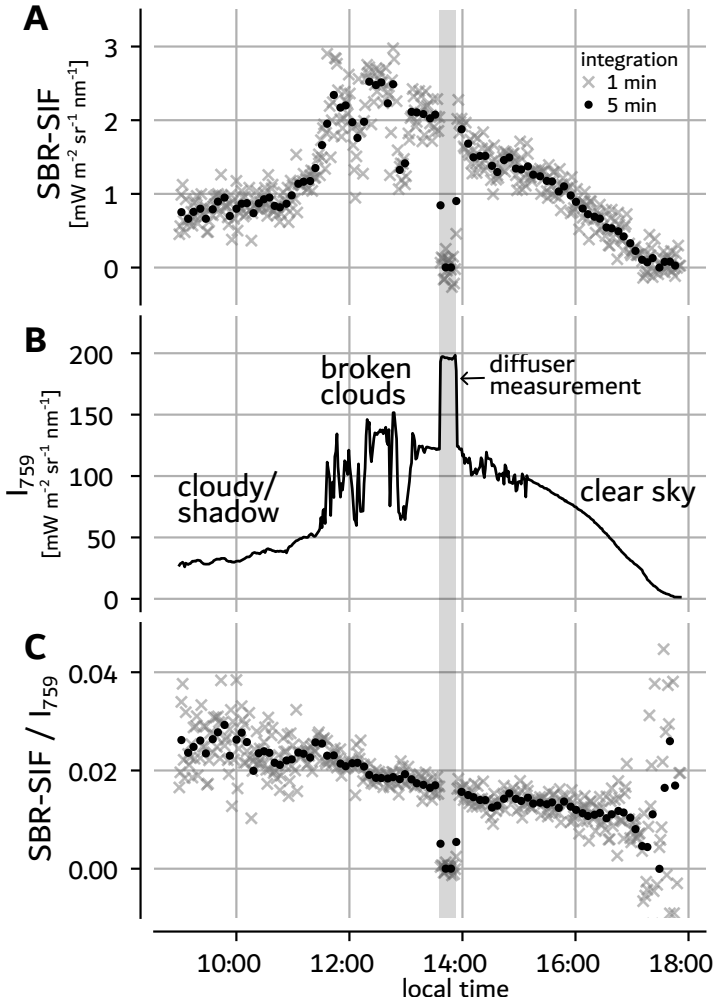

Figure 7: Diurnal SBR-SIF measurement of a peace lily leaf under varying atmospheric conditions. The SBR-SIF signal (A, for 1 and 5 min integration time) follows the changing reflected radiance traced by I_{759} (B). The relative SIF signal (C) is stable with a slight decrease throughout the day, presumably because of plant stress. A diffuser measurement (ca. 13:30) confirms the accurate SIF detection.

remains unaffected by the rapid light variations and stable during the entire measurement period with an almost ideal random noise behavior (Fig. 6B), which corresponds closely to the reported CCD's read out noise. The small positive offset, corresponding to 0.08 $\mathrm{mW\,m^{-2}\,sr^{-1}nm^{-1}}$, could be introduced by residual stray light in the prototype setup. This experiment confirms the absence of any atmospheric influence on proximal SBR-SIF measurements and demonstrates the high stability of the prototype setup, which was not actively stabilized. The corresponding Allan-plot (Fig. 6C) confirms the statistical noise behavior and absence of drifts. The noise-equivalent signal (NES) at an integration time of ca. 3 min is 0.1 $\mathrm{mW\,m^{-2}\,sr^{-1}nm^{-1}}$, which is comparable to precisions state-of-the-art techniques can reach under ideal conditions (Grossmann et al., 2018; Kukkurainen et al., 2025).

4.2.5 SIF diurnal cycle

Finally, to demonstrate the monitoring capabilities of the SBR-SIF we performed measurements of a Peace Lily leaf (Spathiphyllum spp.) throughout a day under varying illumination conditions. The leaf was fixed with its upper side facing the zenith. The fiber was pointed towards the leaf from the top at ca. 10 cm distance and the SBR-SIF signal was averaged over 1 and 5 minutes (with instrument NES of 0.2 and 0.08 $\mathrm{mW\,m^{-2}\,sr^{-1}nm^{-1}}$, respectively, see Fig. 6). In

the morning the sky was overcast and the leaf was in the shade. Therefore, the reflected solar irradiance at 759 nm, I_{759}, was small, and the SBR-SIF signal was only 0.7 - 1 $mW\,m^{-2}\,sr^{-1}nm^{-1}$ (see Fig. 7A,B). Around noon the sun started to shine directly on the leaf, as indicated by the higher I_{759} and the simultaneous increase of SIF to 2 - 2.5 $mW\,m^{-2}\,sr^{-1}nm^{-1}$. During this time a broken cloud cover caused large variations in the incoming solar radiance that are followed by I_{759} and the SBR-SIF signal. At around 13:30 we placed a non-fluorescent diffuser in front of the fiber, confirming the zero signal of the SBR-SIF, while I_{759} increases to its highest value. After 15:00 the sky was clear and the I_{759} showed a smooth decrease until sunset. An examination of the relative SBR-SIF signal, i.e. SBR-SIF/I_{759} (Fig. 7C), shows that the SIF signal follows the radiance of incoming solar radiation during the different illumination conditions of this day. Much of the variability seen in I_{759} is not observed in relative SIF. However, throughout the day relative SIF is decreasing, with values around 0.025 in the morning, 0.02 around noon, and 0.015 around 17:00. This behavior was observed previously (Supplement S7) and is likely caused by a reaction of the leaf to illumination, temperature, and water availability throughout the day under stressful sunny and dry conditions on the roof. Relative SIF also illustrates that during low light conditions in the early morning and evening the 1 min SIF data has high variability that is reduced when the signal is averaged to 5 minutes. This is the expected behavior from measurements that are dominated by statistical uncertainties due to photon shot noise. Only at around 17:00, i.e. at a solar zenith angle of 82.4°, do the 5-min averaged SBR-SIF measurement become noise-dominated. Further averaging, for example to the common 30-minute interval used by eddy covariance CO_2 measurements would further decrease the uncertainty. Overall this test measurement demonstrates that our SBR-SIF prototype is capable of providing real-world scientific SIF monitoring data.

5 Discussion

We have presented the theoretical concept of SBR-SIF and its implementation in a prototype instrument that proved the validity of this new approach to measure SIF from vegetation. Here we discuss the inherent advantages and limitations of SBR-SIF, in particular in comparison to currently used hyperspectral proximal remote sensing measurements of SIF.
SBR-SIF is a direct measurement of SIF, i.e. by using an optical setup that isolates the SIF radiance from all reflected, scattered or direct solar radiation, the SBR measures a light intensity that is directly proportional to the SIF radiance. This leads to the following advantages:

1. *SBR-SIF does not require any signal/data processing beyond the correction of the detector dark signal and a radiometric calibration.* Thus, SBR-SIF avoids complex hyperspectral retrievals to separate the weak SIF radiance from the reflected radiance, as required in current proximal SIF measurements. Consequently, SBR-SIF does not only simplify the quantification of SIF, but also eliminates the systematic errors resulting from the hyperspectral retrievals of SIF (Frankenberg et al., 2011; Grossmann et al., 2018; Chang et al., 2020).

2. *SBR-SIF does not require skylight reference measurements.* Current hyperspectral SIF retrievals require skylight reference spectra alongside the leaf or canopy spectra recorded with the same spectrometer (Meroni et al., 2009; Grossmann et al., 2018). This limits their applicability to setups with a clear view of the sky, i.e. above the canopy. In addition, to eliminate instrument effects in the comparison of reference and plant spectrum, the spectrometer must be actively and precisely temperature-stabilized and/or the skylight measurement must be made very frequently. This increases instrument complexity and reduces the temporal coverage of the SIF observations. SBR-SIF instruments, on the other hand, measure continuously, with each detector exposure providing an independent, direct SIF radiance quantification. Because of this, and its much higher inherent thermal

stability, most SBR-SIF implementations do not need active temperature stabilization. Not requiring skylight references also means that SBR-SIF measurements can be performed from within or below a canopy, opening new opportunities in SIF monitoring and research.

3. *SBR-SIF measurements are not sensitive to changes in atmospheric radiative transfer or illumination conditions.* The need to alternate between leaf/canopy and skylight reference spectra makes current hyperspectral SIF measurements sensitive to the atmospheric state and illumination conditions, especially under cloudy and hazy conditions, when the incoming light radiance and spectrum can change rapidly. Because the SBR-SIF measurement is independent of atmospheric radiative conditions and leaf/canopy reflectivity, uncertainties imposed by illumination effects are mostly eliminated thus increasing the overall accuracy of the SIF measurement.

4. *SBR-SIF instruments feature a simple design and are easy to operate.* As noted above, in contrast to current hyperspectral SIF instruments, SBR-SIF does not require active temperature stabilization. Mechanical and optical components to switch between leaf/canopy and reference measurements are also not required. Thus, SBR-SIF instruments can be more compact, robust, and use less power than current hyperspectral instruments. This simplifies field deployments, and measurement operation, and enables more versatile applications.

A limitation of SBR-SIF measurements is their spectral constraint to strong O_2 lines. While SBR-SIF measurements at lower wavelength in the red (O_2B band) may be possible, the full SIF spectrum, as derived by hyperspectral approaches (Liu et al., 2015), cannot be determined. Moreover, SBR-SIF is not suitable for operation on aircraft and satellites. Its observational range is limited to ca. 50 m due to the reabsorption of the SIF signal by O_2 molecules between the canopy and the instrument. While hyperspectral approaches using the entire O_2A band face similar restrictions, solar Fraunhofer line-based retrievals circumvent this problem.
We demonstrated that our SBR-SIF prototype has similar or higher precision than current proximal SIF systems (ca. $0.1\,\mathrm{mW\,m^{-2}\,sr^{-1}nm^{-1}}$ for 3 min exposure). By minimizing systematic errors, the SBR–SIF approach provides highly accurate SIF data across all atmospheric conditions. Higher precision is achievable through longer integration times and increased light throughput. The substantial simplification of instrumentation, operation and signal processing enables the straightforward implementation of real-time SIF data streams.

6 Conclusion

We present a technique for proximal SIF remote sensing that is based on a fundamentally different concept than current sensors. The SBR-SIF approach relies on the fact that solar light within a saturated oxygen line is completely attenuated by Earth's atmosphere once it reaches a plant at the surface. Consequently, no light is reflected from plants in these saturated lines. SIF emits a smooth spectrum within the the atmospheric O_2A band and is thus the only significant source of light in the saturated line centers. Our theoretical calculations show that measuring the light radiance in a 10 pm wide wavelength window in the O_2 line at 760.65 nm provides a direct quantification of SIF under all conditions anywhere on Earth's surface. The weak SIF radiance, the high reflected light intensity outside of the saturated band, and the very narrow wavelength interval impose strict requirements on to the spectral resolution, contrast and light throughput of a SBR-SIF system. We show that an FPI, used in double-pass configuration, in combination with a narrow prefilter, can fulfill these requirements. We present three possible implementations of an SBR using different prefilters and detector units: monochormator SBR, single-order spectrographic SBR, and multi-order spectrographic SBR, each offering distinct trade-offs in performance, practicality, and additional spectral information.

We developed a prototype based on the multi-order spectrographic SBR implementation. Our measurements demonstrate the following capabilities, which align well with our theoretical predictions:

1. The SBR is able to fully resolve individual saturated O_2 absorption lines (resolving power exceeding 300.000, Sect. 4.2.1).

2. The SBR can isolate the SIF signal from surrounding reflected light. The isolated SIF intensity is visible to the bare eye in the raw data of the SBR detector and can be quantified using simple averaging and correction of the detector's dark signal (Sect. 4.2.2).

3. SBR-SIF observations of the SIF Kautsky effect in a dark-light transition experiment further confirm the direct quantification of SIF (Sect. 4.2.3).

4. Non-fluorescent reflective diffuser observations demonstrate that the SBR-SIF measurements are essentially independent of atmospheric radiative transfer and instrumental effects (Sect. 4.2.4).

5. SBR-SIF can readily be applied in typical proximal SIF monitoring applications (Sect. 4.2.5).

While SBR-SIF measurements are limited to measurements within the O_2A band (and possibly the O_2B band) and an observational range of ca. 50 m, they are a direct quantification of the SIF radiance. Thus, there is no need for recording skylight references or spectral retrievals or atmospheric correction enabling compact, robust and low-power SBR-SIF instruments. Overall, this greatly simplifies measurement procedures while offering highly accurate real-time SIF data. The prototype developed and used in this study is still based on a prefilter (spectrograph) and detector available in our laboratory. Given the systems early development stage, future research and development, e.g. using an interference prefilter and an avalanche photodiode in a monochromator SBR, will further improve the instrument performance, while reducing size and power-consumption. Because the setup of an SBR-SIF system is much simpler, industrial production cost of SBR-SIF instruments will be well below that of current commercial proximal SIF remote sensing systems.
By improving scalability, SBR–SIF enables broader and more wide-spread application of SIF measurements, helping to close key observational gaps, advance understanding of plant and ecosystem processes, and expand their use in areas such as ecosystem monitoring and precision agriculture.

Acknowledgments

We thank SLS Optics Ltd. for manufacturing the etalon and sharing their expertise.

Author contributions

JS and JK conceptualized the research. JK performed the calculations, conceptualized, designed, and manufactured the SBR prototype, conducted and evaluated the measurements, and drafted the manuscript. Both authors contributed to revising the manuscript.

Conflict of interest statement

The authors declare that they have no conflict of interest.

References

C. Y. Chang, L. Guanter, C. Frankenberg, P. Köhler, L. Gu, T. S. Magney, K. Grossmann, and Y. Sun. Systematic assessment of retrieval methods for canopy far-red solar-induced chlorophyll fluorescence using high-frequency automated field spectroscopy. *Journal of Geophysical Research: Biogeosciences*, 125(7):e2019JG005533, 2020. doi: 10.1029/2019JG005533.

R. Doughty, T. P. Kurosu, N. Parazoo, P. Köhler, Y. Wang, Y. Sun, and C. Frankenberg. Global GOSAT, OCO-2, and OCO-3 solar-induced chlorophyll fluorescence datasets. *Earth System Science Data*, 14(4):1513–1529, Apr. 2022. doi: 10.5194/essd-14-1513-2022.

M. Drusch, J. Moreno, U. Del Bello, R. Franco, Y. Goulas, A. Huth, S. Kraft, E. M. Middleton, F. Miglietta, G. Mohammed, L. Nedbal, U. Rascher, D. Schuttemeyer, and W. Verhoef. The FLuorescence EXplorer Mission Concept—ESA's Earth Explorer 8. *IEEE Transactions on Geoscience and Remote Sensing*, 55(3):1273–1284, Mar. 2017. doi: 10.1109/TGRS.2016.2621820.

S. Du, L. Liu, X. Liu, J. Guo, J. Hu, S. Wang, and Y. Zhang. SIFSpec: Measuring Solar-Induced Chlorophyll Fluorescence Observations for Remote Sensing of Photosynthesis. *Sensors*, 19(13):3009, July 2019. doi: 10.3390/s19133009.

C. Fabry and H. Buisson. Wavelength measurements for the establishment of a system of spectroscopic standards. *The Astrophysical Journal*, 27(3):169–196, 1908.

C. Frankenberg and J. Berry. *Solar Induced Chlorophyll Fluorescence: Origins, Relation to Photosynthesis and Retrieval*. Elsevier, 2017. ISBN 978-0-12-409548-9. doi: 10.1016/B978-0-12-409548-9.10632-3.

C. Frankenberg, A. Butz, and G. C. Toon. Disentangling chlorophyll fluorescence from atmospheric scattering effects in O_2 A-band spectra of reflected sun-light: REMOTE SENSING OF CHLOROPHYLL FLUORESCENCE. *Geophysical Research Letters*, 38(3):n/a–n/a, Feb. 2011. doi: 10.1029/2010GL045896.

C. Frankenberg, C. O'Dell, L. Guanter, and J. McDuffie. Remote sensing of near-infrared chlorophyll fluorescence from space in scattering atmospheres: implications for its retrieval and interferences with atmospheric CO2 retrievals. *Atmospheric Measurement Techniques*, 5 (8):2081–2094, 2012. doi: 10.5194/amt-5-2081-2012.

C. Fuchs, J. Kuhn, N. Bobrowski, and U. Platt. Quantitative imaging of volcanic SO2 plumes using Fabry–Pérot interferometer correlation spectroscopy. *Atmospheric Measurement Techniques*, 14(1):295–307, 2021. doi: 10.5194/amt-14-295-2021.

K. Grossmann, C. Frankenberg, T. S. Magney, S. C. Hurlock, U. Seibt, and J. Stutz. PhotoSpec: A new instrument to measure spatially distributed red and far-red Solar-Induced Chlorophyll Fluorescence. *Remote Sensing of Environment*, 216:311–327, 2018. doi: 10.1016/j.rse.2018.07.002.

International Organization for Standardization. Standard atmosphere, 1975. ISO 2533:1975, Geneva.

P. Jacquinot. The Luminosity of Spectrometers with Prisms, Gratings, or Fabry-Perot Etalons. *Journal of the Optical Society of America*, 44(10):761, 1954. doi: 10.1364/josa.44.000761.

P. Jacquinot. New developments in interference spectroscopy. *Reports on Progress in Physics*, 23(1):267–312, 1960. doi: 10.1088/0034-4885/23/1/305.

H. Kautsky and A. Hirsch. Neue Versuche zur Kohlensäureassimilation. *Die Naturwissenschaften*, 19(48):964–964, Nov. 1931. doi: 10.1007/BF01516164.

J. Kuhn. Trace gas imaging in the atmosphere with a Fabry–Pérot interferometer - a case study for sulfur dioxide. Master's thesis, Heidelberg University Library, 2015. doi: 10.11588/HEIDOK.00029948.

J. Kuhn, N. Bobrowski, T. Wagner, and U. Platt. Mobile and high-spectral-resolution Fabry–Pérot interferometer spectrographs for atmospheric remote sensing. *Atmospheric Measurement Techniques*, 14(12):7873–7892, 2021. doi: 10.5194/amt-14-7873-2021.

J. Kuhn, N. Bobrowski, G. Boudoire, S. Calabrese, G. Giuffrida, M. Liuzzo, K. Karume, D. Tedesco, T. Wagner, and U. Platt. High-spectral-resolution Fabry-Pérot interferometers overcome fundamental limitations of present volcanic gas remote sensing techniques. *Frontiers in Earth Science*, 11:1039093, Mar. 2023. doi: 10.3389/feart.2023.1039093.

A. Kukkurainen, A. Lipponen, V. Kolehmainen, A. Arola, S. Cogliati, and N. Sabater. SIFFI: Bayesian solar-induced fluorescence retrieval algorithm for remote sensing of vegetation. *Remote Sensing of Environment*, 318:114558, Mar. 2025. doi: 10.1016/j.rse.2024.114558.

H. K. Lichtenthaler and U. Rinderle. The Role of Chlorophyll Fluorescence in The Detection of Stress Conditions in Plants. *CRC Critical Reviews in Analytical Chemistry*, 19(sup1):S29–S85, Jan. 1988. doi: 10.1080/15476510.1988.10401466.

X. Liu and L. Liu. Influence of the canopy BRDF characteristics and illumination conditions on the retrieval of solar-induced chlorophyll fluorescence. *International Journal of Remote Sensing*, 39(6):1782–1799, Mar. 2018. doi: 10.1080/01431161.2017.1404165.

X. Liu, L. Liu, S. Zhang, and X. Zhou. New Spectral Fitting Method for Full-Spectrum Solar-Induced Chlorophyll Fluorescence Retrieval Based on Principal Components Analysis. *Remote Sensing*, 7(8):10626–10645, Aug. 2015. doi: 10.3390/rs70810626.

Y.-S. Lv, P.-H. Xie, J. Xu, Y.-T. Li, and H.-R. Zhang. Effective transmittance of Fabry–Perot cavity under non-parallel beam incidence. *Chinese Physics B*, 33(1):014210, Jan. 2024. doi: 10.1088/1674-1056/ad0ec3.

J. K. Marrs, T. S. Jones, D. W. Allen, and L. R. Hutyra. Instrumentation sensitivities for tower-based solar-induced fluorescence measurements. *Remote Sensing of Environment*, 259: 112413, June 2021. doi: 10.1016/j.rse.2021.112413.

M. Meroni, M. Rossini, L. Guanter, L. Alonso, U. Rascher, R. Colombo, and J. Moreno. Remote sensing of solar-induced chlorophyll fluorescence: Review of methods and applications. *Remote Sensing of Environment*, 113(10):2037–2051, 2009. doi: 10.1016/j.rse.2009.05.003.

G. H. Mohammed, R. Colombo, E. M. Middleton, U. Rascher, C. Van Der Tol, L. Nedbal, Y. Goulas, O. Pérez-Priego, A. Damm, M. Meroni, J. Joiner, S. Cogliati, W. Verhoef, Z. Malenovský, J.-P. Gastellu-Etchegorry, J. R. Miller, L. Guanter, J. Moreno, I. Moya, J. A. Berry, C. Frankenberg, and P. J. Zarco-Tejada. Remote sensing of solar-induced chlorophyll fluorescence (SIF) in vegetation: 50 years of progress. *Remote Sensing of Environment*, 231: 111177, Sept. 2019. doi: 10.1016/j.rse.2019.04.030.

A. Perot and C. Fabry. On the Application of Interference Phenomena to the Solution of Various Problems of Spectroscopy and Metrology. *The Astrophysical Journal*, 9:87, Feb. 1899. doi: 10.1086/140557.

Z. A. Pierrat, T. S. Magney, W. P. Richardson, B. R. K. Runkle, J. L. Diehl, X. Yang, W. Woodgate, W. K. Smith, M. R. Johnston, Y. R. S. Ginting, G. Koren, L. P. Albert, C. L. Kibler, B. E. Morgan, M. Barnes, A. Uscanga, C. Devine, M. Javadian, K. Meza, T. Julitta, G. Tagliabue, M. P. Dannenberg, M. Antala, C. Y. S. Wong, A. L. D. Santos, K. Hufkens, J. K. Marrs, A. E. L. Stovall, Y. Liu, J. B. Fisher, J. A. Gamon, and K. Cawse-Nicholson. Proximal remote sensing: An essential tool for bridging the gap between high-resolution ecosystem monitoring and global ecology. *New Phytologist*, 246(2):419–436, Apr. 2025. doi: 10.1111/nph.20405.

J. A. Plascyk. The MK II Fraunhofer Line Discriminator (FLD-II) for Airborne and Orbital Remote Sensing of Solar-Stimulated Luminescence. *Optical Engineering*, 14(4), Aug. 1975. doi: 10.1117/12.7971842.

A. Porcar-Castell, E. Tyystjärvi, J. Atherton, C. Van Der Tol, J. Flexas, E. E. Pfündel, J. Moreno, C. Frankenberg, and J. A. Berry. Linking chlorophyll a fluorescence to photosynthesis for remote sensing applications: Mechanisms and challenges. *Journal of Experimental Botany*, 65(15):4065–4095, Aug. 2014. doi: 10.1093/jxb/eru191.

J. Qin, Z. Deng, S. Wang, J. Chen, P. Fu, and C. Huang. A review on solar-induced chlorophyll fluorescence of vegetation and its ecological process modeling. *Ecological Frontiers*, 46(1): 55–67, Feb. 2026. doi: 10.1016/j.ecofro.2025.09.015.

L. S. Rothman, I. E. Gordon, Y. Babikov, A. Barbe, D. C. Benner, P. F. Bernath, M. Birk, L. Bizzocchi, V. Boudon, L. R. Brown, A. Campargue, K. Chance, E. A. Cohen, L. H. Coudert, V. M. Devi, B. J. Drouin, A. Fayt, J.-M. Flaud, R. R. Gamache, J. J. Harrison, J.-M. Hartmann, C. Hill, J. T. Hodges, D. Jacquemart, A. Jolly, J. Lamouroux, R. J. L. Roy, G. Li, D. A. Long, O. M. Lyulin, C. J. Mackie, S. T. Massie, S. Mikhailenko, H. S. P. Müller, O. V. Naumenko, A. V. Nikitin, J. Orphal, V. Perevalov, A. Perrin, E. R. Polovtseva, C. Richard, M. A. H. Smith, E. Starikova, K. Sung, S. Tashkun, J. Tennyson, G. C. Toon, V. G. Tyuterev, and G. Wagner. The HITRAN2012 molecular spectroscopic database. *Journal of Quantitative Spectroscopy and Radiative Transfer*, 130:4–50, 2013. doi: 10.1016/j.jqsrt.2013.07.002.

G. C. Toon. Solar Line List for the TCCON 2014 Data Release, 2015.

S. A. Trim and A. Hueni. Spectroradiometric calibration and temperature sensitivity analysis of a fluorescence box. *Applied Optics*, 64(24):7197, Aug. 2025. doi: 10.1364/AO.564003.

M. Vaughan. *The Fabry-Perot Interferometer History, Theory, Practice and Applications*. CRC Press, Boca Raton, 1989. ISBN 978-0-85274-138-2.

J. Wu, N. Prohaska, M. Hough, A. John, J. Garnello, and S. Saleska. Leaf spectral reflectance of tropical plants growing in Biosphere 2. `https://ecosis.org/package/leaf-spectral-reflectance-of-tropical-plants-growing-in-biosphere-2` (last accessed: 2026-04-20).

Supplementary Material for: Direct quantification of solar-induced chlorophyll fluorescence using compact solar-blind optical radiometers

Jonas Kuhn[1,⋆] and Jochen Stutz

Department of Atmospheric and Oceanic Sciences, University of California, Math Sciences Building 7127, Los Angeles, CA 90095, USA

[1]now at: Institute of Environmental Physics, Heidelberg University, Im Neuenheimer Feld 229, 69120 Heidelberg, Germany

⋆Corresponding author: jonaskuhn-sci@posteo.de

S1 O_2 line width and visible range

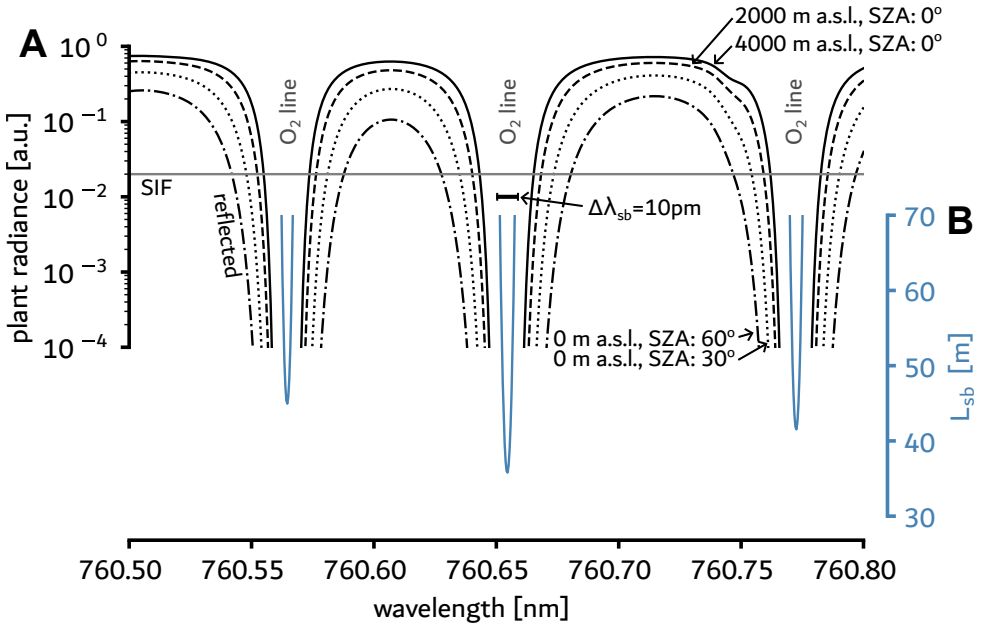

Figure S1: The width of strong saturated O_2 lines depends on their optical depth, and thus, on the solar zenith angle (SZA) and the surface altitude above sea level (A). Re-absorption of the SIF signal by O_2 between the emitting canopy and the instrument limits the range of SBR-SIF measurements.

S2 SBR-SIF can not be implemented with grating-based monochromators

Grating spectrographs are widely used in the current SIF measurement approaches. The compact spectrographs used in field measurements typically have a resolution of 0.3 nm at 760 nm (Grossmann et al., 2018; Trim and Hueni, 2025), which is less by choice, but rather due to the compromise between light-throughput and instrument size, as determined by the grating dispersion (Kuhn et al., 2021). A grating-based spectrograph or monochormator with an etendue of $E = 10^{-4}\,\mathrm{sr\,mm^2}$ would require an entrance slit width $w_S \approx \sqrt{E} = 0.01\,\mathrm{mm}$, which, in order to achieve $\delta\lambda_{SBR} = 0.0033\,\mathrm{nm}$ at $\lambda = 760\,\mathrm{nm}$ requires a focal length f_{GS} of (see (Kuhn et al., 2021) for details)

$$f_{GS} \approx \frac{\lambda}{\delta\lambda_{SBR}} w_S \approx 2.3\,\mathrm{m} \tag{S1}$$

Grating monochromators with these specifications have been manufactured, however they are expensive and their application in environmental field measurements of SIF is not practical, because their volume is on the order of 1 $\mathrm{m^3}$, they weigh several 100 kg.

S3 FPI double pass configuration is sufficient for SBR-SIF implementation

Figure S2A shows the plant radiance (sum of reflected light and SIF contribution) close to strong saturated O_2 lines. The wings of a spectral FPI transmittance peak S2B fall of too slowly, in order to sufficiently suppress the reflected light radiance in the SBR measurement S2C. This problem is solved with a double pass FPI configuration (inset in S2B), which provides sufficient

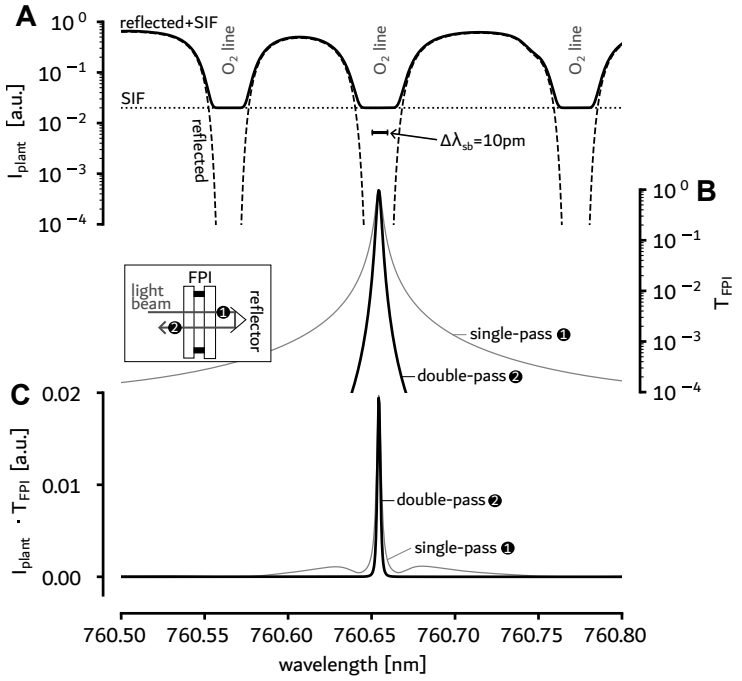

Figure S2: A: In narrow spectral windows $\Delta\lambda_{\mathrm{sb}}$ within individual strong O_2 lines the outgoing radiation from a plant or leaf is determined only by SIF. FPIs have sufficient resolving power to filter out $\Delta\lambda_{\mathrm{sb}}$ from the total outgoing spectral radiation and thus enable the direct measurement of SIF (B). The FPI should thereby be used in a double-pass configuration (inset in panel B) for improved spectral contrast (C).

spectral contrast to isolate the SIF radiance inside the O_2 line from all reflected light, realizing an SBR.

S4 Pressure and temperature dependence of an ASE

The FPI used in this study is an ASE with ultra low thermal expansion glass spacers (linear thermal expansion coefficient of $< 2 \cdot 10^{-8}\,\mathrm{K}^{-1}$). The spectral shift of the FPI transmittance peak of the order $m = \frac{\Gamma}{\lambda_m}$ introduced by a change in the optical path between the two mirrors is given by:

$$\frac{\mathrm{d}}{\mathrm{d}(nd)}\lambda_m \approx \frac{1}{m}\frac{\mathrm{d}}{\mathrm{d}(nd)}\Gamma \approx \frac{2}{m} \tag{S2}$$

Accordingly, the change in the optical path $\Delta(dn)$ related to a spectral shift of one FWHM of the FPI transmittance peak $\delta\lambda_{\mathrm{FPI}}$ for an ASE with specifications as in Sect. 3.3 is:

$$\Delta(dn) = \frac{m}{2}\delta\lambda_{\mathrm{FPI}} \approx 2.17\,nm \tag{S3}$$

Consequently, the thermal expansion of the spacers of ca. $0.01\,\mathrm{nm\,K}^{-1}$ can be neglected in most environments. The main temperature and pressure dependence of the ASE is caused by changes in the refractive index of the gas in between the two mirrors, which is air in our case. The refractive index is mostly controlled by the density of air, which can be approximated via the ideal gas law:

$$(n-1) \propto \frac{p}{T} \tag{S4}$$

According, to equation S3, a refractive index change by ca. $4{\cdot}10^{-6}$ causes a spectral shift of the FPI transmittance spectrum by $\delta\lambda_{FPI}$, which corresponds to $\frac{\Delta(n-1)}{(n-1)} \approx 1.5\%$, and consequently $\Delta p \approx 15\,\mathrm{hPa}$ or $\Delta T \approx -4.5\,\mathrm{K}$. These condition changes lay well in the range of the expected

pressure and temperature variability during environmental measurements. Hermetically sealing the ASE, i.e. stabilizing the air density inside the ASE, provides a simple solution to this problem and leads to negligible dependence of the FPI's properties on the common variability in environmental conditions.

S5 Simulation of the intensity distribution in the focal plane of the SBR

Our forward model of the SBR instrument is based on former work by (Kuhn, 2015; Kuhn et al., 2021) and described in detail in (Kuhn et al., 2023). For each pixel, we calculate the transmittance spectrum of the instrument, which is determined by the product of FPI spectral transmittance (which is squared to account for the double pass configuration) and prefilter spectral transmittance. The spectrum of incoming light (see Sect. 2.2 of the main text) is then multiplied with the transmittance spectrum of each pixel, resulting in the simulated relative intensity distribution on the focal plane detector.

S6 Radiometric calibration

The radiometric calibration of the SBR-SIF prototype was conducted as follows:

1. We used a calibrated light source (HL-3 PLUS-CAL by Ocean Optics) with a cosine corrector connected to the SBR fiber and irradiance-calibrated the SBR in the detector region (I_{759}) marked in Fig. 5A, i.e., in a spectral region unaffected by O_2 absorption and less than 2 nm from the SBR spectral range.

2. Using the calibrated setup with the cosine corrector pointed to the sky zenith, we measured the sky irradiance E_{sky} during a clear day, with low variation of the sky brightness.

3. Immediately after that, we removed the cosine corrector and pointed the fiber on a calibrated diffuser plate (Spectralon, R=0.99). The radiance I_d of the diffuser plate is then given by:
$$I_{\mathrm{d}} = \frac{R\,E_{\mathrm{sky}}}{\pi} \tag{S5}$$

4. The measurement of the diffuser plate is then used to derive the calibration factor f_{cal}:
$$f_{\mathrm{cal}} = \frac{I_{\mathrm{d}}}{I_{759}} \tag{S6}$$

For the configuration of the prototype used in all measurements presented in the paper $f_{\mathrm{cal}} = 15.7(\pm 20\%)\,\mathrm{mW\,m^{-2}\,sr^{-1}\,nm^{-1}\,s\,DU^{-1}}$.

S7 Peace Lily relative SIF measured with the Photospec instrument

Grossmann et al. (2018) performed a diurnal SIF measurement of a Peace Lily plant with their Photospec instrument in Oct. 2016 (see Fig. 9 in Grossmann et al., 2018). The plant species, measurement location, and illumination conditions were the same or similar to our diurnal SBR-SIF measurement in Figure 7. Figure S3 shows the relative SIF signal corresponding to the Photospec observations shown in Figure 9 of Grossmann et al. (2018), which also declines throughout the day. This confirms our SBR-SIF relative SIF result in Figure 7.

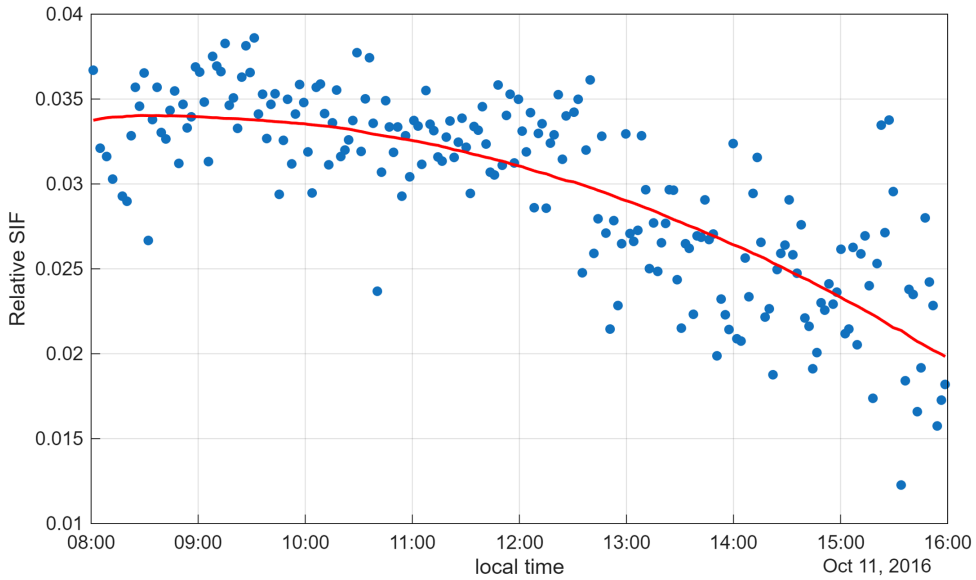

Figure S3: Diurnal decay of the relative SIF signal of a peace lily plant measured under similar conditions with the photospec instrument (Grossmann et al., 2018).